Nuclear Science and Techniques (2026) 37:98
https://doi.org/10.1007/s41365-026-01912-7

Effectiveness of calibration and correction algorithms on a prototype of the POLAR-2/LPD detector

Di-Fan Yi[1,2] · Qian Liu[1] · Hong-Bang Liu[2] · Fei Xie[2] · Huan-Bo Feng[2] · Zu-ke Feng[2] · Jin Li[3] · En-Wei Liang[2] · Yang-Heng Zheng[1]

Received: 22 February 2024 / Revised: 9 September 2024 / Accepted: 30 October 2024 / Published online: 24 March 2026

Abstract
Gaseous X-ray polarimetry refers to a class of detectors used to measure the polarization of soft X-rays. The systematic effects of such detectors introduce residual modulation, which leads to systematic biases in the polarization detection results of the source. This paper discusses the systematic effects and their calibration and correction using a Gas Microchannel Plate–Pixel Detector (GMPD) prototype for the POLAR-2/Low-Energy X-ray Polarization Detector (LPD). Additionally, we propose an algorithm that combines parameterization with Monte Carlo simulation and Bayesian iteration to eliminate residual modulation. The residual modulation after data correction at different energy points was reduced to less than 1%, and a good linear relationship was observed between the degree of polarization and the modulation factor. The improvement in the degree of modulation after correction ranged from 2% to 15%, and the results exceeded those of the Imaging X-Ray Polarimetry Explorer (IXPE) above 5 keV.

Keywords Gaseous X-ray polarimetry · Residual modulation · Bayesian approach

1 Introduction

POLAR-2 [1] is a gamma-ray burst (GRB) [2] polarization measurement project that will be conducted in 2026 on the Chinese Space Station following POLAR [3] through collaboration between China and Europe. This project aims to answer the most important questions in astrophysics regarding the nature of GRBs, including understanding the mechanisms that propel energetic jets, elucidating the processes responsible for energy dissipation, determining the composition of jets, investigating the configurations of magnetic fields, and unraveling the mechanisms behind particle acceleration and radiation [4–8]. The detection of polarization in GRBs plays a crucial role in providing important clues to address the aforementioned problems [9–14].

In this project, the LPD [15], a sub-payload of POLAR-2, is the first large-field-of-view soft X-ray polarimeter dominantly developed by Chinese scientists. The GMPD [16] is an innovative gaseous pixel detector developed to validate the design of the POLAR-2/LPD payload.

Recently launched polarimetric detectors, such as PolarLight [17–21], IXPE [22], CXPD-01 [23], the underdeveloped eXTP [24, 25], CATCH type-A [26], and POLAR-2/LPD all utilize gaseous pixel polarimetric detector structures. This type of detector has high spatial resolution and is capable of imaging electron tracks at the level of hundreds of micrometers, thus providing excellent sensitivity for polarimetric detection. However, owing to the complex and sophisticated structure of the gaseous pixel detector, as well as its high spatial resolution sensitivity, the operational state of the instrument, various components, and electronic devices may introduce systematic effects on the polarimetric detection results. These systematic effects can result

This work was supported by the National Key R&D Program of China (No. 2022YFA1602204), the National Natural Science Foundation of China (Nos. 12175241, 12221005, and 12027803), and the Fundamental Research Funds for the Central Universities.

✉ Qian Liu
liuqian@ucas.ac.cn

1 School of Physical Science, University of Chinese Academy of Sciences, Beijing 100049, China

2 School of Physical Science and Technology, Guangxi University, Nanning 530004, China

3 Institute of High Energy Physics, Chinese Academy of Sciences, Beijing 100049, China

in nonzero modulation, called residual modulation, when detecting unpolarized sources, leading to systematic biases in the measurement of polarized sources. As low-energy electron tracks are relatively short, the residual modulation effects produced by these systematic effects are more significant in low-energy events and cannot be ignored.

For residual modulation, IXPE employs two correction methods [27]: The first involves oscillating the detector during the detection process to integrate and eliminate some of the systematic effects. The second method involves calibrating the corresponding Stokes parameters [28] q and u for systematic effects in different regions and energy points and then subtracting them on an event-by-event basis to eliminate systematic effects. However, the second correction is only applicable to on-axis X-ray polarization observations, as continuing to use the Stokes parameters to describe the observation results in off-axis cases is difficult. For the first large-field-of-view soft X-ray polarimeter, the majority of observations of POLAR-2/LPD will be conducted in off-axis scenarios. Therefore, in this paper, we discuss the research and correction of residual modulation in GMPD and propose an innovative correction algorithm that can be extended to correct residual modulation in off-axis scenarios. Through research and correction, the polarization detection capability of the GMPD detector has exceeded that of IXPE at energies above 5 keV, making it one of the best-performing soft X-ray polarimeters currently available. This advancement will aid POLAR-2/LPD in obtaining high-precision and accurate observational results during its on-orbit mission.

In this paper, we introduce the basic structure and polarization detection principles of POLAR-2/LPD in Sect. 2. We then discuss the residual modulation caused by signal response and its correction methods in Sect. 3. In Sect. 4, we discuss the residual modulation caused by geometric effects and propose a modulation curve correction method based on the parameterization of scale ratios, combined with Monte Carlo simulation and Bayesian iteration [29] (see Appendix A), and provide the errors of this algorithm. Subsequently, we compare various data reconstruction characteristics before and after the algorithm correction with the modulation calibrated by the IXPE detector. Finally, in Sect. 5, we discuss the performance of the GMPD after correction, emphasizing the performance and scalability of the correction algorithm, and outline prospects of future research.

2 Geometric structure and working principle of LPD

The LPD system shown in Fig. 1 is composed of a total of nine detector modules, arranged in a 3×3 array configuration. Each detector module consists of nine detection units with 90° field of view (FoV), resulting in 81 detection units. A detection unit of the LPD consists of a working gas, gas

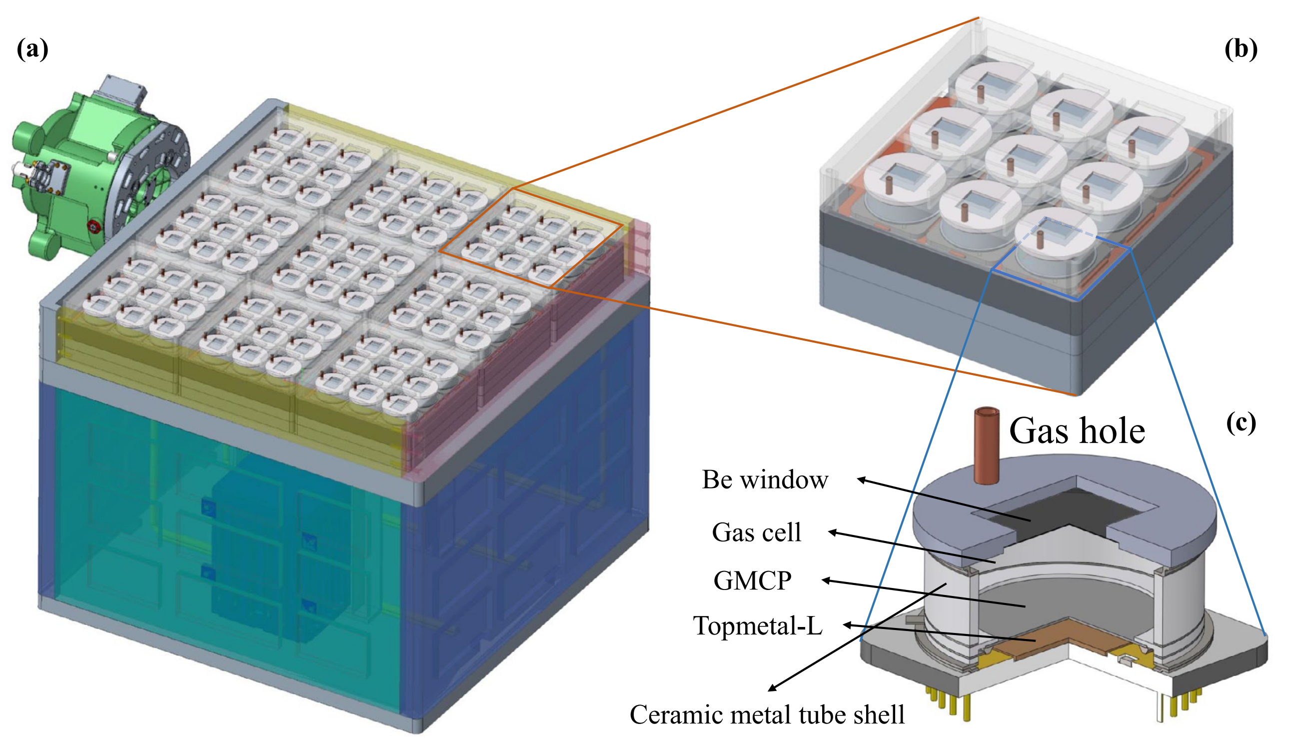

Fig. 1 (Color online) Mechanical structures of the LPD. **a** LPD payload. **b** Detector array module. **c** Detector unit

microchannel plate (GMCP) [30], pixel readout chip, and frame structure. The gas filled in the detector consists of a volume ratio of 3:2 of dimethyl ether (DME) and helium (He) at a pressure of 0.8 atmospheres, serving the purpose of photoelectric effects and formation of ionization tracks. The upper end of the gas chamber was sealed with a 50 µm beryllium window, which prevents the entry of lower-energy photons and ensures gas containment to prevent leakage. A GMCP layer is positioned near the bottom plane of the chamber for electron avalanche multiplication. The bottom of the chamber is a Topmetal-L chip specifically designed for the LPD within the Topmetal chip series [31–34]. It features a 356×512 pixel array with a pixel size of 45 µm and supports readout modes in the rolling shutter and region of interest. Additionally, it has low power consumption (0.8W). Note that the prototype LPD discussed in this paper uses the Topmetal-II chip [35], which operates on the same principles and pixel structure as Topmetal-L. However, the array size is 72×72, with a pixel scale of 83 µm. Topmetal-L will be an iteratively upgraded chip based on Topmetal-II, where "L" represents large and low power consumption. The intended chip version, Topmetal-L, which is expected to be formally integrated into the LPD, will be optimized in terms of power consumption, effective area, and resolution based on the existing chip version, Topmetal-II.

The soft X-rays (Fig. 2) pass through the beryllium window of the detector unit and have a certain probability of undergoing photoelectric effects within the drift region, resulting in the generation of photoelectrons. These photoelectrons carry the polarization information of the incident photons. Photoelectrons deposit ionization energy within the gas and generate secondary ionization electrons until they completely stop. Secondary electrons are multiplied by transferring them to the holes inside the GMCP under a drift electric field of 1 keV/cm in the drift region. Within the induction region, an upward-directed electric field is applied, causing some of the secondary ionization electrons to drift downward onto the surface of the GMCP. Some of these electrons enter the micro-channels and undergo avalanche multiplication. The multiplied electrons then emerge from the lower surface of the GMCP, where some are absorbed, resulting in the production of a pulse signal. The remaining multiplied electrons continue to drift toward the Topmetal chip, inducing signals in the corresponding pixels. This process projects photoelectron tracks onto the 2D plane of the Topmetal chip, ultimately producing an energy-deposition projection image of the track.

Generally, the angular distribution of photoelectrons detected by the gaseous pixel detector is modulated using polarized X-rays. In gaseous pixel detectors, photons primarily interact with the K-shell electrons of gas molecules through photoelectric interactions, and the direction of the

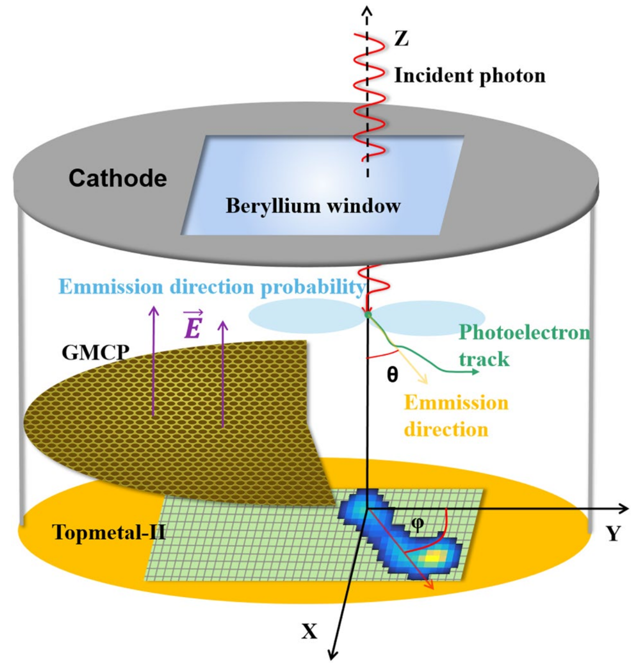

Fig. 2 (Color online) Polarization detection principle of GMPD

emitted electrons is described by the differential cross section according to the following formula [36]:

$$\frac{d\sigma^k}{d\Omega} \propto \frac{\sin^2\theta\cos^2\phi}{(1+\beta\cos\theta)^2}, \tag{1}$$

where β is the emission velocity of the photoelectron in units of the speed of light, and c, θ and ϕ are the latitude and azimuthal angles, respectively. Because of the lack of resolution in the Z direction for the LPD, we reconstruct [37, 38] the 2D projection angular distribution of the azimuthal angle of the emitted photoelectron, corresponding to the integration of θ in the formula. Therefore, the reconstructed angular distribution is modulated by $\cos^2$. In theory, for 100% polarized X-rays, the minimum value of the true emission distribution in ϕ should be zero. However, owing to the limitations in instrument resolution, system effects, and reconstruction algorithm accuracy, there was a certain proportion of unmodulated components in the angular distribution, as shown in Fig. 3a and b. Therefore, the modulation function of ϕ, $M(\phi)$ can be written as:

$$M(\phi) = A + B\cos^2(\phi - \phi_0), \tag{2}$$

where ϕ_0 denotes the polarization phase of the source. The degree of modulation μ is defined as the ratio of the area occupied by the modulation component in the distribution:

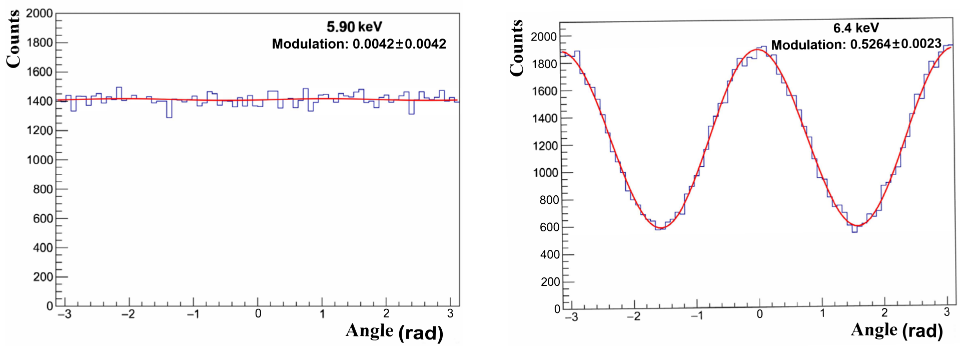

(a) (b)

Fig. 3 (Color online) **a** Modulation curves for unpolarized 5.90 keV X-rays. **b** Polarized 6.40 keV X-rays with polarization angle at 0°

$$\mu = \frac{B}{2A + B}. \tag{3}$$

When the source is fully linearly polarized, the degree of modulation is referred to as the modulation factor, which characterizes the sensitivity of the detector to polarized sources.

3 Calibration and correction of signal response

The structural design and operational principles of GMPD result in variations in the response between pixels, which can affect the energy resolution of the detector. More importantly, some of these factors can introduce anisotropic differences, leading to residual modulations. This section discusses the impact and calibration of these factors.

3.1 Pixel response differences

Owing to the subtle structural differences between each pixel, uniformity of the electric field, and uniformity of the GMCP gain, the signal induction intensity of the drift charge varies among different pixels. The relative signal induction intensity on each pixel should be calibrated. We uniformly irradiate using a 4.51 keV flat source and statistically record the signal distribution received by each pixel. Because the response curve of the pixels exhibits good linearity [39], we can characterize the relative signal induction intensity of a pixel using the mean of the signal distribution received on that pixel. We accumulated more than 100,000 valid signals for each pixel to reduce the impact of statistical fluctuations. For each pixel, we calculated the average value of the trigger signals exceeding 5 sigma above the noise level and used this average value to characterize the charge induction coefficient of that pixel. We corrected the readout results for each pixel based on the relative magnitudes of the induction coefficients between different pixels. Figure 4 illustrates the average distribution of pixel ADC values before and after correction.

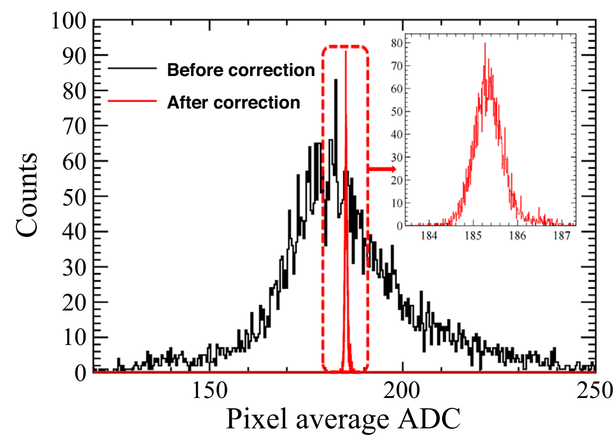

Fig. 4 (Color online) Distribution of pixel average ADC values before and after correction, with black representing the pre-correction values and red representing the post-correction values

3.2 Rolling-shutter and signal decay

Another source of residual modulation is the attenuation of the pixel signal amplitude caused by the signal readout time delay. Because Topmetal adopts a rolling-shutter readout method to read each frame of the image, pixel signals are read out in sequence, which means that a certain delay results from the triggering of the induction signal to the readout, and a delay also occurs in the readout time of different pixels on the same track. The charge-sensitive Preamplifier (CSA) structure of Topmetal-II is shown in Fig. 5a. A CSA includes a differential amplifier, sub-threshold nMOS resistor, and feedback capacitor, where the pixel controls the discharge of the induced charge through the drain voltage. Therefore, the scanned readout signal is attenuated compared with the true signal amplitude at the triggering moment owing to the time delay. The scanning time for one frame of Topmetal-II

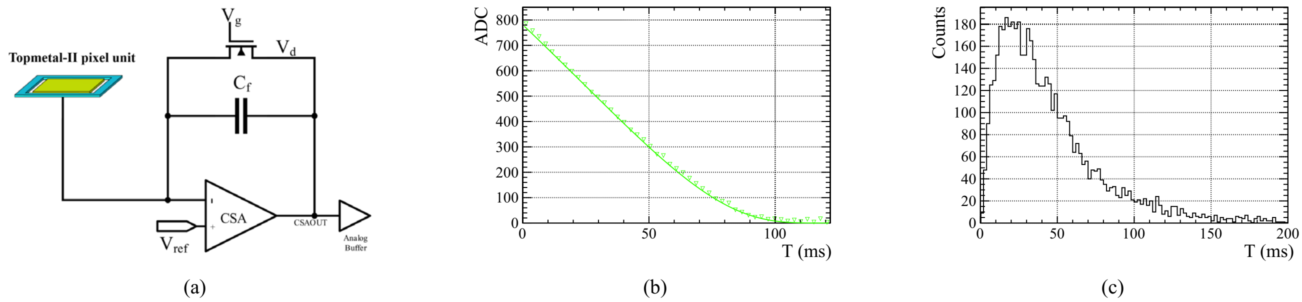

Fig. 5 (Color online) **a** Topmetal-II pixel CSA structure. The green portion represents the top metal, which is used to induce the drift charge signal. C_f denotes the feedback capacitor. V_g represents the gate voltage, V_d represents the drain voltage, and V_{ref} represents the amplifier's reference voltage. **b** Trend and fitting curve of pixel ADC value decay over time. **c** Distribution of decay time for all pixels, where the decay time of a pixel is defined as the time interval for the pixel signal value to decay from *a* to *a*/2

is $\tau_{\text{frame}} = 2.59$ ms, and the scanning time interval for each pixel is $\tau_{\text{pixel}} = 500$ ns. Owing to the rolling-shutter method of scanning the chip column-by-column along the 0° direction, the scanning time interval between adjacent pixels in the 90° direction is 35 μs, whereas that between adjacent pixels in the 0° direction is 500 ns, with $\Delta T_{0^\circ} \ll \Delta T_{90^\circ}$. The difference in the scanning time intervals between 0° and 90° can result in inconsistent signal attenuation gradients in these two directions, introducing a vertical bias, namely residual modulation in the 90° direction.

To calibrate the systematic errors caused during the scanning process, we must first calibrate the signal attenuation behavior of each pixel and then determine the time difference between each triggered and readout pixel. We input square-wave signals to the chip and record the output results of the pixel readout signals for multiple consecutive frames to obtain the decay characteristics of each pixel and perform parameter fitting. The theoretical formula for the pixel decay is given by Eq. (4):

$$A(t) = a \cdot \exp\left(-\frac{t}{b \cdot t + c}\right). \tag{4}$$

Figure 5b shows the decay pattern of the signal intensity over time on a pixel and the fitting results. Figure 5c shows the decay time distribution of all the pixels on Topmetal-II, indicating that the most likely decay time for a pixel is 20 ms.

The time precision of the GMCP is 10 ns [39], which is significantly smaller than the most likely decay timescale of the pixel. We can obtain the arrival time of the event signal at GMCP by comparing the GMCP trigger signal with the Topmetal-II trigger signal. Because the distance between the GMCP and Topmetal-II chips is only 3.4 mm, the typical time scale for the electron multiplied by the GMCP to traverse this distance is on the order of tens of nanoseconds, which can be neglected compared with the characteristic time scale of the pixel decay. Therefore, we assume that the time of arrival of the multiplied electrons in Topmetal-II is $T_{\text{Arrival}} = T_{\text{GMCP}}$. Denoting the time corresponding to the Topmetal-II trigger frame as T_{Top}, if $T_{\text{Top}} > T_{\text{GMCP}}$, the position scanned has already passed through the region reached by the photoelectrons when the signal arrived. In this case, for the k-th fired pixel, the time difference between the signal triggering and readout is $\Delta t = T_{\text{Top}} - T_{\text{GMCP}} + \tau_{\text{pixel}} \times \text{ID}_k$, where ID_k is the index of the k-th fired pixel. If $T_{\text{Top}} < T_{\text{GMCP}}$, the scanned position has not yet passed through the region reached by the photoelectrons when the signal arrives. In this case, the time difference is $\Delta t = T_{\text{GMCP}} - T_{\text{Top}} + \tau_{\text{pixel}} \times \text{ID}_k$. Based on the time difference, we can then correct the decay signal for each pixel using the following formulas:

$$A_{\text{truth}} = a \cdot \exp\left(-\frac{t_0 - \Delta t}{b \cdot (t_0 - \Delta t) + c}\right), \tag{5}$$

$$t_0 = \frac{c}{1 - b \cdot \log(\frac{a}{A_{\text{out}}})}. \tag{6}$$

3.3 Charge build-up effect

The encapsulated detector exhibits an initial stage in which the gain increases with the accumulated number of events, as illustrated in Fig. 6a. This effect is attributed to charge accumulation. The surface of the Topmetal-II utilized in the detector features a grid-like insulating layer, causing electrons to fall and become adsorbed on this layer, resulting in limited mobility. As the accumulation of avalanche-multiplied electrons increases, the potential on the chip surface gradually changes, impacting the charge collection efficiency and modifying the gain, as shown in Fig. 6b.

If the charge accumulation process is unevenly distributed on the chip surface, it leads to a noticeable signal intensity gradient on the chip surface, eventually resulting in pseudo-modulation perpendicular to the gradient

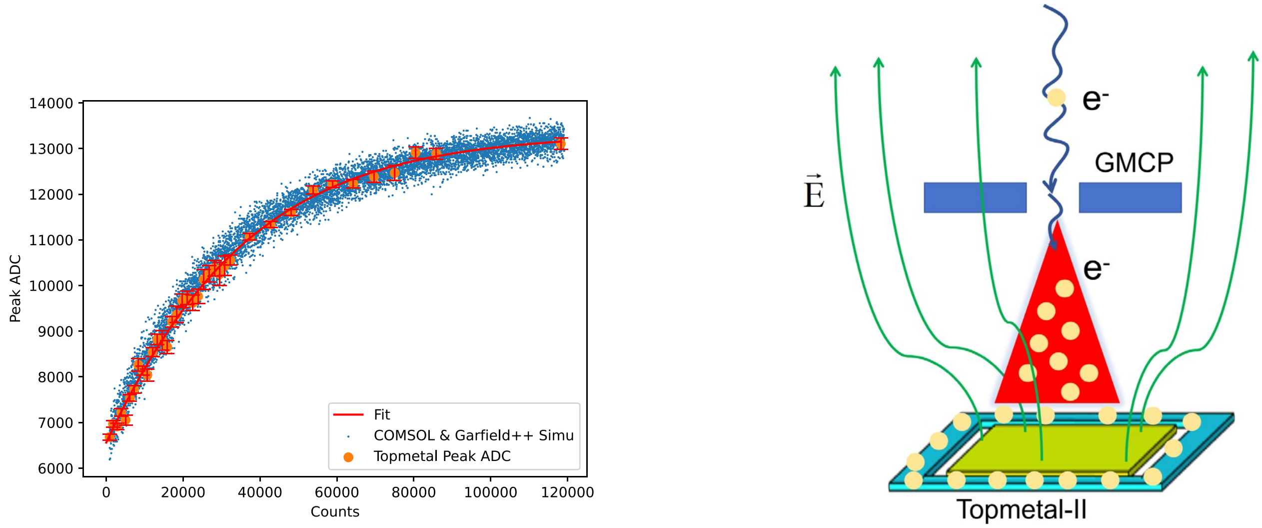

(a) (b)

Fig. 6 (Color online) **a** Variation in chip collection efficiency with the accumulation of events. The orange points represent experimental data results of 4.51 keV photoelectron track energy deposition, characterized by fitting the peak ADC of the data spectrum to represent the variation in chip charge collection efficiency. The blue points represent the trend of collection efficiency variation obtained from the joint simulation using COMSOL and GARFIELD++. **b** Charge accumulation schematic: Electrons accumulate on the insulating layer, forming a low potential region around the top metal. This leads to the formation of a funnel-shaped electric field above the top metal, thereby enhancing the charge collection efficiency of the pixel

direction. Figure 7 illustrates the residual modulation caused by the charge accumulation effect. Initially, a ferrous strip was used to partially obstruct a section of the field of view of the detector, leaving a gap of a few millimeters. Following a 2-h exposure to an X-ray flat source, the obstruction was removed, and a 5.90 keV unpolarized ^{55}Fe source was used to irradiate and collect the photoelectron tracks. After reconstruction, as shown in Fig. 7a, the signal gain at the previous narrow-gap position was significantly higher than that in the shaded area, and the residual

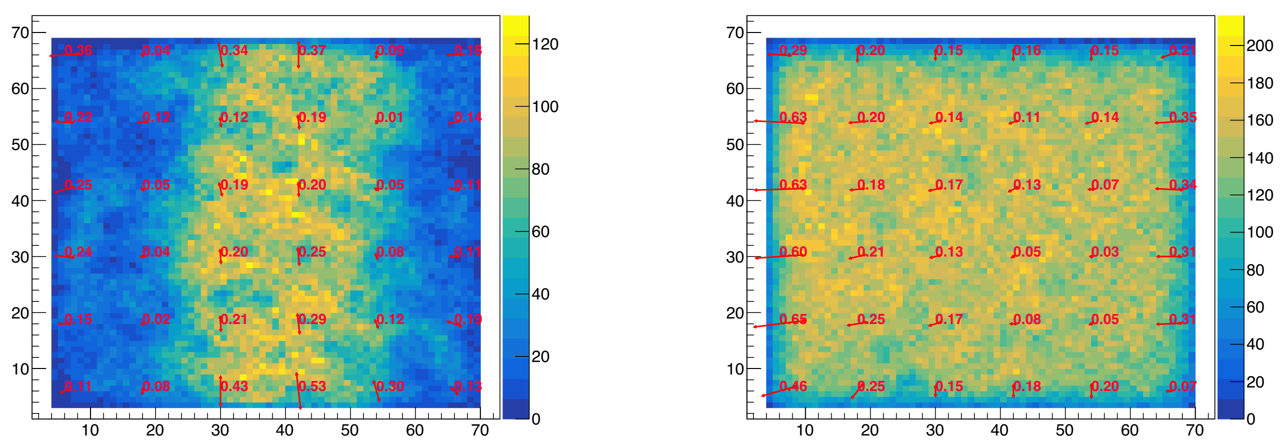

(a) (b)

Fig. 7 (Color online) Residual modulation distribution in different regions of the detector, with each small region composed of 12×12 pixels. **a** Residual modulation distribution of 5.90 keV ^{55}Fe tracks after uneven charge accumulation due to narrow-gap obstruction. **b** Residual modulation distribution of 5.90 keV ^{55}Fe tracks after uniform charge accumulation after the removal of the narrow-gap obstruction. The heatmap represents the distribution of the reconstructed photoelectron emission positions of the tracks, with the direction of the red lines indicating the direction of residual modulation. The length of the line and the adjacent number represent the value of the residual modulation

modulation in the narrow-gap area was higher than that in the shaded area, with the modulation direction parallel to the gap. Subsequently, without any obstruction, the X-ray flat source was used again for 4 h to accumulate charges on the entire surface of the chip to near saturation. The detector was then irradiated with 5.90 keV unpolarized ^{55}Fe, and the tracks were reconstructed, as shown in Fig. 7b. By comparing the results of the ^{55}Fe measurements before and after the charge accumulation reached saturation, we found that the residual modulation caused by the uneven gain due to charge accumulation decreased significantly. Therefore, the impact of the charge accumulation effect can be mitigated by calibrating or measuring the detector after saturating the charge accumulation before conducting the experiments. Because the accumulated charge is unlikely to dissipate naturally once the detector is encapsulated, only a single thorough charge accumulation is required.

By employing Garfield++ and COMSOL for the charge drift accumulation iteration and updating the drift electric field, we successfully replicated this effect in simulations, as indicated by the blue data points in Fig. 6a, which agrees with the experimentally observed gain variations. The charge accumulation process can be described by a simplified Eq. 7, where n is the number of events, q is the accumulated charge on the chip, $q_{\max}$ is the maximum saturated accumulated charge, and α_c is the charge-adsorption coefficient. Therefore, the change in the accumulated charge quantity with respect to the detector count, $q(n)$, can be expressed in a parametric form, as given in Eq. 8.

$$\frac{dq(n)}{dn} = \alpha_c \left(1 - \frac{q(n)}{q_{\max}}\right), \tag{7}$$

$$q(n) = x_0 + x_1 \exp(x_2(n + x_3)). \tag{8}$$

Both the experimental and simulation results indicated that the charge accumulation process gradually reaches saturation, leading to a stable final gain. Additionally, the non-focusing observation mode of the LPD can prevent the uneven accumulation of charge on the chip surface. Therefore, after a sufficient number of accumulated events, the impact of pseudo-modulation caused by the charge accumulation effect in the encapsulated detection unit can be reduced to a negligible level.

4 Calibration and correction of geometrical effects

4.1 Pixelization influence

As shown in Fig. 8a, we considered a shorter track with a circular projection. Owing to the parallel arrangement of Topmetal-II chips in the X- and Y-directions, the signal distribution sensed on the chip pixels exhibits anisotropy for such tracks. The symmetry is most pronounced in the directions of 0° and 90°, which are aligned with the pixel arrangement. The commonly used moment analysis algorithm for shorter tracks calculates the centroid line of the pixel track to determine the direction of electron emission. This can lead to a bias in the reconstruction direction of these tracks toward 0° and 90°.

To mitigate the residual modulation caused by the pixel arrangement, we must exclude events with too few responsive pixels and events that are too short or circular during event selection. Therefore, during reconstruction, we only select events with a number of hit pixels greater than or equal to 27 and exclude the bottom 20% of events with smaller ellipticities. Figure 8b shows the angular distribution of the reconstructed unbiased events before and after the event selection. After event selection, the residual modulation caused by the pixel arrangement is significantly improved.

4.2 Truncation effect

Similarly, because of the rolling-shutter line-by-line scanning readout of the chip, if an event occurs precisely at the position covered by the pixels being scanned at that moment, it will be truncated and appear in both the preceding and subsequent frames. If the truncated part in one frame has fewer fired pixels that do not exceed the threshold, we obtain only an incompletely truncated event. As the edge of the truncated track is always parallel to the scanning direction, a systematic bias is introduced in the scan direction.

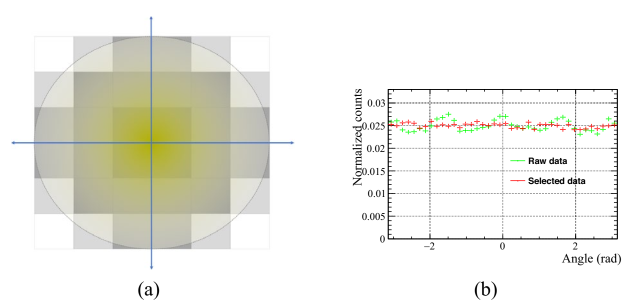

Fig. 8 (Color online) **a** Shorter circular tracks projected onto the readout Topmetal-II chip, where the pixel grayscale represents the signal intensity, with darker colors indicating stronger signals. The axis represents the direction obtained from track reconstruction. The pixel size is 83 μm. **b** Angular distribution of reconstructed electron tracks at 2.98 keV, with a gas environment consisting of a 40% volume fraction of helium gas and 60% dimethyl ether (DME) at 0.7 atm. The green data points represent the reconstruction results without any filtering based on the number of triggered pixels and ellipticity. The red data points represent the filtered results, excluding events with a number of triggered pixels less than 27 and the bottom 20% of events with smaller ellipticity

Therefore, the truncated instances must be selected and filtered. Although most truncated tracks exhibit clearly defined edges, this feature is insufficient for identifying truncated instances, particularly for shorter tracks at lower energies. Thus, we continue to utilize the time information from GMCP and Topmetal-II to determine if an instance is truncated. The time difference recorded by Topmetal-II and GMCP is $\Delta T_{\mathrm{Diff}} = T_{\mathrm{Top}} - T_{\mathrm{GMCP}}$.

- When $\Delta T_{\mathrm{Diff}} < 0$, the pixel ID scanned when the signal arrives is $\mathrm{ID}_{\mathrm{Pixel}} = \frac{\Delta T_{\mathrm{Diff}}}{\tau_{\mathrm{pixel}}}$.
- When $\Delta T_{\mathrm{Diff}} > 0$, the signal actually arrives and is read by Topmetal-II in the second frame. Therefore, the pixel ID scanned when the signal arrives is $\mathrm{ID}_{\mathrm{Pixel}} = 72 \times 72 - \frac{\Delta T_{\mathrm{Diff}}}{\tau_{\mathrm{pixel}}}$.

Considering the combined time resolution of GMCP and Topmetal-II as 262 ns [39] and τ_{pixel}, we determine whether a track is truncated by examining whether the pixel scanned when the signal arrives and the positions of the five pixels before and after it precisely overlap with the region covered by the photoelectron track signal.

Figure 9a and b depict the reconstructed results of the complete and truncated events, respectively, under scanning. Figure 9c shows the reconstructed angle distribution of truncated events in the unpolarized 5.90 keV dataset selected by the algorithm. A significant bias is observed in the direction of ±90°.

4.3 Track image distortion

Excluding the systematic effects and corrections discussed above, the angular reconstruction of the track data obtained from the detector still exhibits residual modulation. This can be partly attributed to the geometry and potential distribution of the detector. The gas cavity of the LPD detection unit is not completely symmetrical. As shown in Fig. 10, in addition to the charge induction chip Topmetal, a temperature and pressure sensor chip is placed nearby. This placement leads to a relatively significant distortion of the electric field near the side of the Topmetal chip adjacent to the sensor chip, resulting in a noticeably higher residual modulation on that side. Furthermore, a 1 mm wide and 0.8 mm deep groove exists between the charge induction collection plane of the Topmetal chip and the base plane of the detection unit. Additionally, several to a dozen bonding wires are present around the chip. The geometric structure of the edge of the chip and potential on the bonding wires also distort the

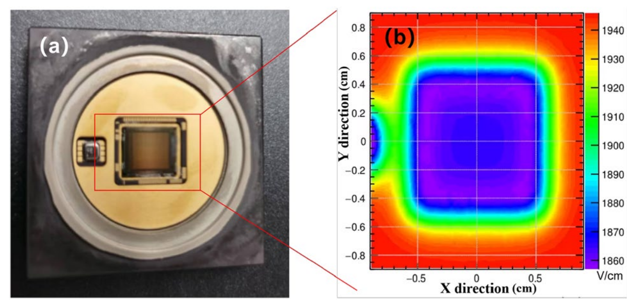

Fig. 10 (Color online) **a** Physical diagram of the detector unit base, with the larger central chip being the Topmetal-II charge induction chip, and the smaller chip on the left being the temperature and pressure sensing chip. **b** Simulation results of the electric field near the detector base. Owing to the structural characteristics of the pressure sensing chip, the overall geometric structure of the detection unit exhibits a certain degree of asymmetry, leading to some distortion in the electric field

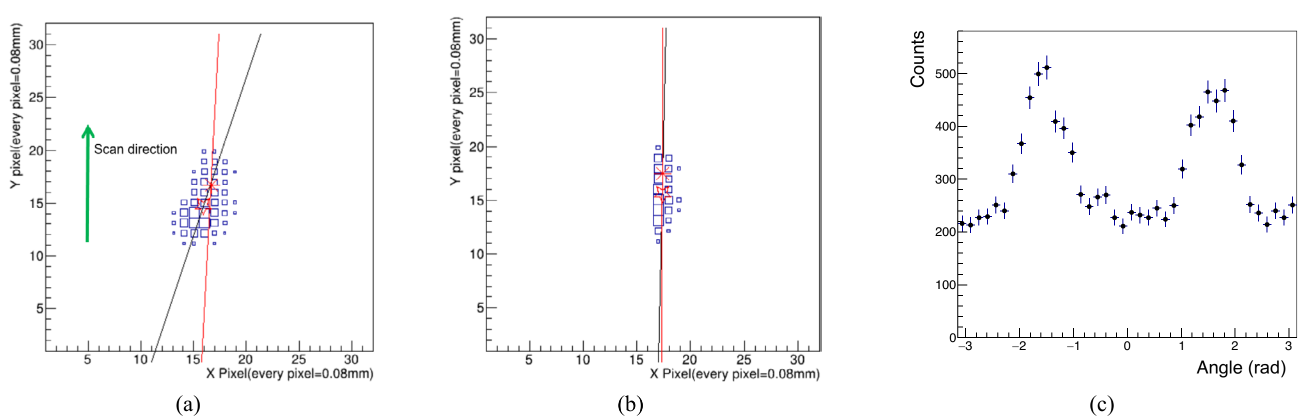

Fig. 9 (Color online) Track truncation. The scale of the box represents the strength of the signal at that pixel. The red star denotes the reconstructed centroid position of the track, whereas the black line represents the reconstructed centroid line direction, which corresponds to the reconstructed azimuthal angle of the photoelectron emission. The red line divides the track into the energy deposition part of the Bragg peak and the initial position part of the photoelectric interaction. **a** Complete track. **b** Truncated track. **c** Reconstructed angular distribution of selected truncated events

electric field at the edge of the chip. Consequently, the direction of the residual modulation reconstructed in the edge portion of Fig. 7 is generally perpendicular to the edge of the chip. Therefore, to minimize the influence of edge electric field distortion on the reconstruction, we opt to exclude events within 12 pixels of the charge center distance from the edge when selecting valid events.

The residual modulation distribution in different regions near the center of the chip appears to be more random. This variability in the residual modulation in certain regions may result from systematic process problems during chip etching, subtle irregularities during detector installation, and uneven charge accumulation, resulting in differences in the electric field across different areas of the chip. These problems can affect the electric-field distribution near the chip surface, and the distortion of the electric field can alter the track shape. This alteration is often nonlinear, and its impact on tracks at different positions, heights, and lengths varies. Consequently, we lack sufficiently precise information to perform pixel-by-pixel or event-by-event corrections from a first-principles perspective for the tracks obtained in the experiment.

The deformation of the tracks is reflected in the differences in the position resolution in different directions of the detector. As shown in Fig. 11, at different energy points, the position resolution in the X direction of the detector is worse than that in the Y direction. This indicates that the distortion of the track is more severe in the X direction. This anisotropic deformation of the tracks leads to excessive stretching in the X direction, resulting in significant residual modulation.

Similar residual modulation challenges also occur in the IXPE detector. The correction scheme for the residual modulation provided by IXPE involves calibrating the experimental scales for each chip region to correct the Stokes parameters required for event reconstruction. Because the IXPE detector must image the observed objects, different regions must be segmented and corrected. However, for the LPD, which lacks imaging capabilities, photons from the source fall uniformly on the entire chip surface. Therefore, the LPD only needs to consider correcting the distribution of the residual modulation integrated over the entire chip surface for events. To address this, we propose a Bayesian method combined with Monte Carlo simulations to correct the residual modulation.

4.3.1 Correction algorithm

When correcting the data for an energy point, we need only calibrate the correction parameter η, which is the ratio of the pixel size in the Y direction to the pixel size in the X direction. We can phenomenologically explain the need to introduce η: The distortion of the electric field causes the

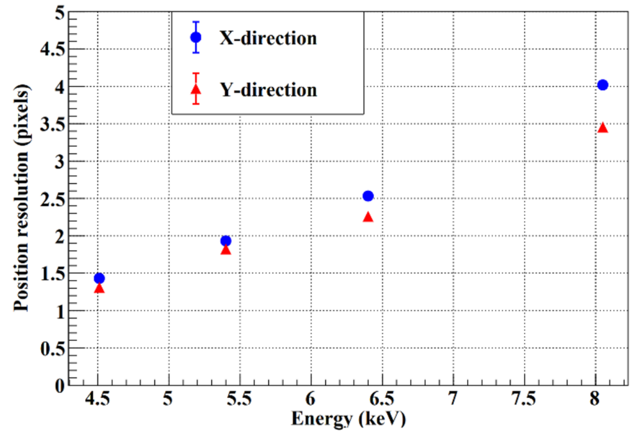

Fig. 11 (Color online) Position resolution of GMPD of varying energies. Circular markers depict the results in the X direction, whereas triangular markers represent the results in the Y direction

equipotential surfaces to no longer be parallel to the Topmetal chip plane. Therefore, by projecting the chip plane onto the deformed equipotential surface, the linearity in different chip directions has different scaling rates. We select the ratio of the scaling rates calibrated in the two directions parallel and perpendicular to the scanning direction as η. Note that the η values differed for different regions of the chip. However, because the LPD does not have polarized imaging capabilities, the correction parameter we consider is the weighted average value $\bar{\eta}$ of the parameters for different chip regions.

Calibrating $\bar{\eta}$ requires a comparison of experimental data and simulations. Taking the 5.40 keV energy point as an example [40], we calibrated the modulation curves obtained from a 99.9% polarized source at 0°, 30°, 60°, 90°, 120°, and 150° polarization phases. Owing to the residual modulation, significant differences are observed in the modulation at these phases, with a difference of approximately 18% between the modulations at 0° and 90°, as shown in Sect. 4.3.2. Because residual modulation is an inherent property of the detector and is independent of the polarization phase of the source, the overall measured modulation curve is a result of the superposition of the residual modulation and source modulation. Therefore, the overall modulation curve can be described as

$$M_{\mathrm{Obs}}(\phi) = M_{\mathrm{Res}}(\phi) \cdot M_{\mathrm{Source}}(\phi, \phi_0), \tag{9}$$

where M_{Obs} is the modulation curve obtained from the reconstructed angular distribution data, M_{Res} represents the impact of the residual modulation, and M_{Source} is the modulation curve generated by the polarized source. Under normal incidence, the form of M_{Source} is

$$M_{\mathrm{Source}}(\phi, \phi_0) = A \cos^2 (\phi - \phi_0) + B. \tag{10}$$

According to Eq. 10, we observe that M_{Source} is modulated by $\cos^2$. Therefore, by combining the two sets of data equally with a 90° difference in the polarization phase, the modulation caused by the polarized source can be eliminated. Thus, when six sets of data are mixed equally in 0°, 30°, 60°, 90°, 120°, and 150° polarization phases, the modulation curve of the angular distribution $M_{\text{Obs}} \propto M_{\text{Res}}$. The modulation distributions of the combined data are shown in Fig. 12. The combined results indicate that the residual modulation distribution still follows Eq. 10, and fitting different combined datasets within the error range shows that the residual modulation values obtained from different datasets are consistent, with the phase of the residual modulation being 0°.

We obtained the residual modulation amplitude at the 5.40 keV energy point by fitting the residual modulation curve shown in Fig. 12d. Next, we used simulations to reproduce the same residual modulation distribution and obtain a response matrix to correct the residual modulation in the experimental data. We utilized the software framework star-XP [41] specifically designed for the LPD. The simulation framework meticulously simulates the interaction processes between the photoelectrons and the detector, as well as the digitization process. The simulated data output of the framework agreed well with the experimental data. The operational procedure followed the steps described below:

1. In the simulation framework, we simulated the tracks of 1.5 million unpolarized 5.40 keV X-ray photons and maintained the parameters set in the simulator consistent with the actual operating parameters of the detector.
2. Initially, we set $\bar{\eta}$=1, representing the state of the detector without electric field distortion, and simulated the two-dimensional image of the photoelectron tracks after digitization. We reconstructed each of the 1,500,000 tracks without distortion to obtain the reconstructed angle information, $\text{Angle}_{\text{Truth}}$. Note that this is not the true value of the emission angle of the photoelectrons provided by the simulation, but rather the angle value obtained from the reconstruction. The distribution of $\text{Angle}_{\text{Truth}}$ is shown in Fig. 13a.
3. In the simulation, we adjusted the value of $\bar{\eta}$ to deviate from 1, representing the occurrence of electric field distortion in the detector. We used the photoelectron track simulations from Step 1 after digitization, and owing to different scaling in the X and Y directions, the reconstructed angle distribution, $\text{Angle}_{\text{Distor}}$, exhibited a nonzero residual modulation. When $\bar{\eta}$ <1, the phase of the residual modulation was 0°, consistent with the experimental data. By adjusting the value of $\bar{\eta}$, we aligned the modulation amplitude of the $\text{Angle}_{\text{Distor}}$ distribution with Fig. 12d, as shown in Fig. 13(b). For 5.40 keV, the value of $\bar{\eta}$ was determined to be 0.981.
4. Combining the $\text{Angle}_{\text{Truth}}$ and $\text{Angle}_{\text{Distor}}$ reconstructed step by step in the second and third steps, we obtained the response matrix M_{Distor}, which resulted from the adjustment of the parameter $\bar{\eta}$. The physical interpreta-

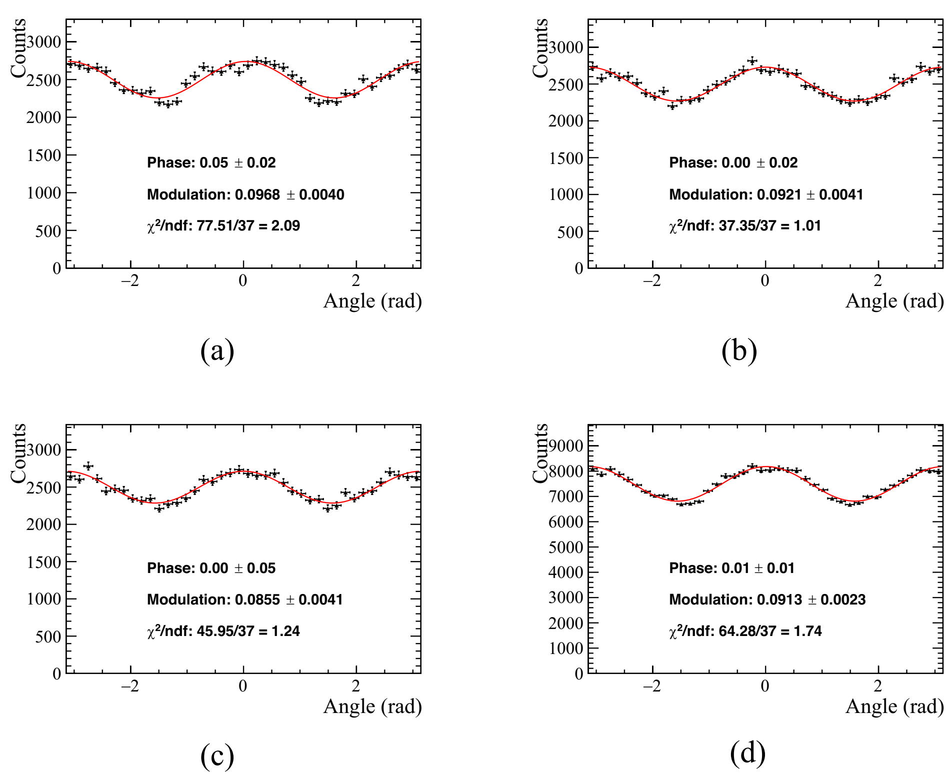

Fig. 12 (Color online) Combination results of data at different polarization phases for 5.40 keV. **a** Combining polarization data at 0° and 90°; **b** combining polarization data at 30° and 120°; **c** combining polarization data at 60° and 150°; **d** combining polarization data at 0°, 30°, 60°, 90°, 120°, and 150°

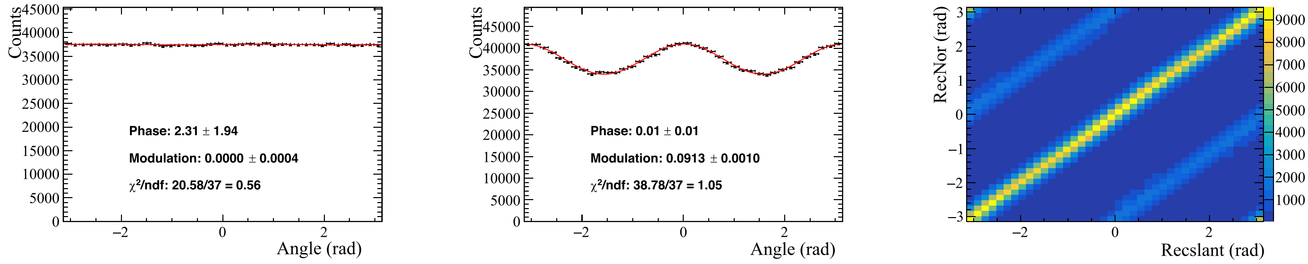

(a) $\bar{\eta}$=1 (b) $\bar{\eta}$=0.981 (c) M_{Distor}

Fig. 13 (Color online) **a** Distribution of $\text{Angle}_{\text{Truth}}$, with the red line representing the fitted modulation curve, exhibiting a modulation degree of 0. **b** Distribution of $\text{Angle}_{\text{Distor}}$, with the modulation degree adjusted by tuning $\bar{\eta}$ to match the experimental data in Fig. 12d. **c** Response matrix, with the ordinate representing the reconstructed angles of events at $\bar{\eta}$ = 1, and the abscissa representing the reconstructed angles of events at $\bar{\eta} = 0.981$

tion of M_{Distor} is as follows: If we denote N_i^{Truth} as the number of instances for which the reconstructed angle falls within the i-th bin when $\bar{\eta}$=1, then the number of instances for the same events after adjusting $\bar{\eta}$ and reconstructed within the j-th bin is given by Eq. 11. In other words, the element (m, n) of M_{Distor} is proportional to the probability value $P(n|m)$: The probability that an event originally reconstructed in the m-th bin is reconstructed in the n-th bin owing to the adjustment of $\bar{\eta}$.

$$N_j^{\text{Distor}} = \Sigma_i N_i^{\text{Truth}} \cdot M_{ij} \tag{11}$$

After obtaining the parameter $\bar{\eta} = 1$ that describes the system effect and its corresponding response matrix M_{Distor}, we employed a Bayesian iterative process algorithm to decouple the modulation distribution generated by the polarization source, which does not exhibit an electric field distortion, from the overall system effects. Many software packages offer Bayesian algorithm capabilities, and in our study, we utilized the RooUnfoldBayes packages integrated within RooUnfold [42]. The RooUnfoldBayes package can iteratively restore the input angular modulation distribution to its undistorted state based on the provided response matrix M_{Distor} and automatically calculate the errors for each bin following the Bayesian iteration process.

The use of Bayesian methods involves the selection of prior distributions and adjustment of the number of iterations. First, owing to the periodicity of the modulation curves with a period of π, monotonically increasing or decreasing distributions are inappropriate. Therefore, for simplicity, we set the prior distributions to be uniform. Second, with respect to the number of iterations, we determine the convergence of the iteration process by comparing the χ^2 values of the distributions $M(\phi)_{n+1}$ and $M(\phi)_n$ after the $(n+1)$-th and n-th iterations. We found that when the number of iterations was set to 10, the χ^2 values for different phases, polarizations, and energies were all less than 0.5, indicating that the iterative process essentially reached convergence. Additionally, after 10 iterations, the introduced iteration errors in each bin were relatively small. Therefore, we set the number of iterations to 10. Figure 14a illustrates the variation in the χ^2 values corresponding to different numbers of iterations, whereas Figs. 14b and 14c present the corrected results for the 5.40 keV 99.9% polarized data for 0° and 90° phases, respectively.

4.3.2 Result

At a specific energy point, using the aforementioned method, we need only calibrate one corresponding parameter, namely $\bar{\eta}$, and simulate the response matrix at that energy point. This enables the application of Bayesian iterations to correct the modulation curves at different degrees of polarization and phases. The corrected polarization degree and modulation level exhibit a good linear relationship, and the modulation levels at different phases show good consistency. Figure 15 compares the modulation distribution before and after correction of the experimental data in 5.40 keV and 90° polarization phases, ranging from unpolarized to 99.9% polarization. When the degree of polarization is low, the residual modulation will dominate the distribution of the modulation curve. At this point, the unrevised experimental data reconstruction results will exhibit significant deviations. In contrast, the corrected data maintain good stability in the reconstruction of the polarization phase while exhibiting a strong linear relationship between the modulation level and polarization degree. Figure 16 compares the experimental data before and after correction at several energy points, including 2.98 keV, 4.51 keV, 5.40 keV, 6.40 keV, and 8.05 keV, for different polarization phases and degrees. The uncorrected data, because the residual modulation is not eliminated, exhibit significant differences in the reconstructed modulation degree at different phases. For example, at 4.51 keV, the degrees of modulation at 0° and 90° for the same fully polarized source differ by approximately

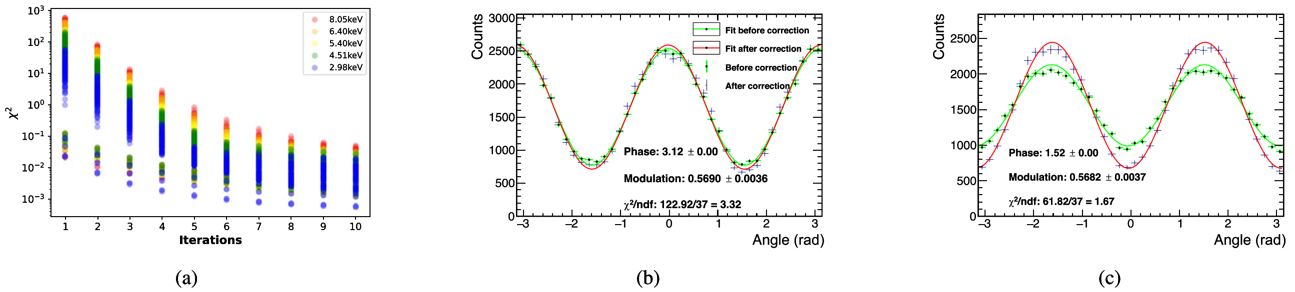

Fig. 14 (Color online) **a** χ^2 variation of the distributions after 1–10 Bayesian iterations for different polarization degrees and polarization phases at different energy points. After 10 iterations, the χ^2 values are all less than 0.5, indicating that the Bayesian iterations have essentially converged. **b** and **c**, respectively, show the completely polarized data at 5.40 keV and 0°, 90° phases. The green curve represents the original measured reconstructed angular distribution, whereas the blue curve represents the distribution after 10 Bayesian iterations. A comparison between **b** and **c** reveals that the Bayesian iterations have corrected the modulation levels at the two phases to the same level

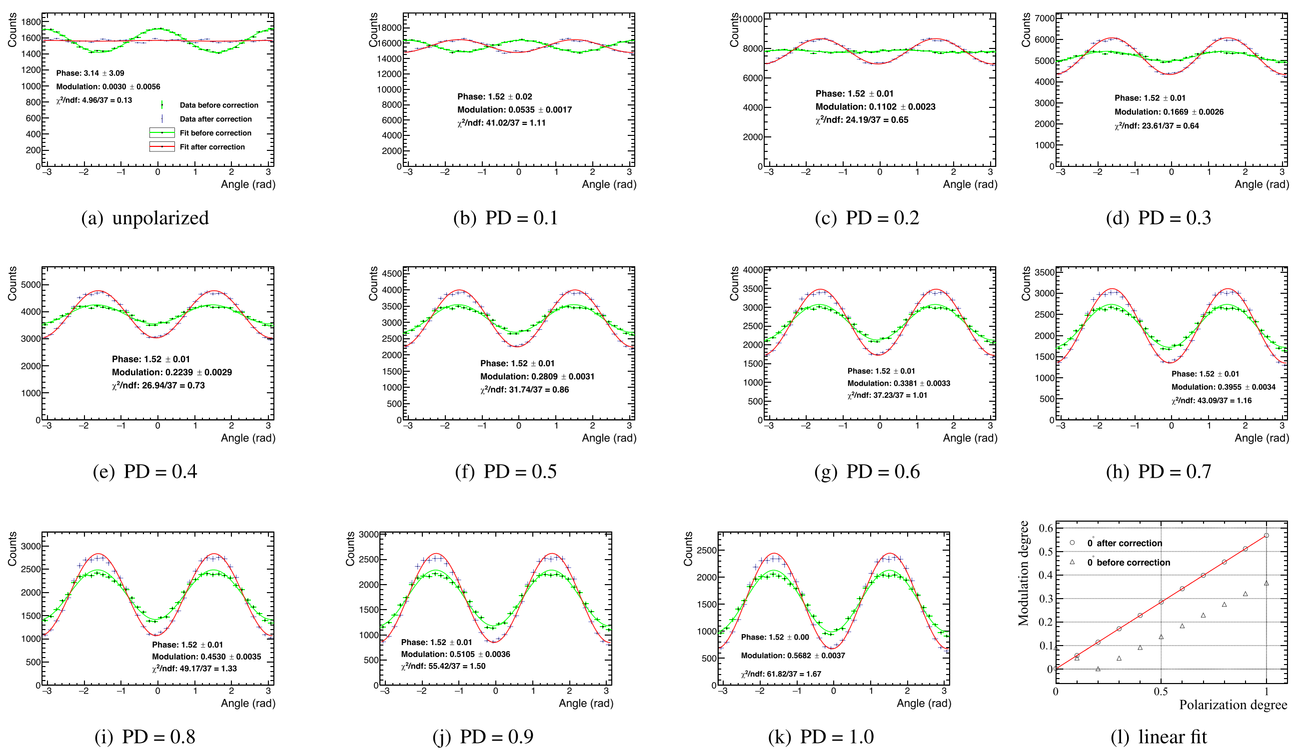

Fig. 15 (Color online) **a**–**k** Comparison of modulation degrees before and after correction for experimental data at 5.40 keV and 90° polarization phases for different polarization degrees where PD represents the polarization degree. The legend is the same as in Fig. 14. The unpolarized data were obtained by mixing datasets with a 90° phase difference using the method described at Fig. 12, and the datasets for different polarization degrees were obtained by proportionally mixing unpolarized and fully polarized data. **l** The triangle represents the relationship between the modulation degree reconstructed from experimental data before correction and the polarization degree, whereas the circle represents the relationship after correction, and the red line represents the fitted curve of the corrected data points

18%. The polarization phase reconstruction results from the uncorrected data also show a significant deviation from the true values, particularly in the direction that differs by 90° from the polarization direction of the residual modulation. However, after Bayesian iterative correction, the polarization data show good consistency in the degree of modulation across different phases. Additionally, the polarization and modulation degrees exhibit a good proportional relationship, satisfying the calibration requirements of the LPD.

4.3.3 Error and comparison

The error in the degree of modulation of the corrected data distribution occurs primarily from two sources. The first part originates from the statistical error in the data, which can be obtained by fitting. The other part of the error results from the use of the Bayesian method for correction:

1. Error propagation in the Bayesian iteration process: This error can be calculated through the error propagation matrix A4.
2. Termination of the Bayesian iteration: Although the chi-square calculation results exhibit good convergence after 10 iterations for all experimental data, the convergence levels of the data at different polarization phases are inconsistent owing to the fixed number of iterations. This results in slight differences in the reconstructed modulation degree at different polarization phases after correction.
3. Parameterized response matrix: The error in the estimation of the parameter $\bar{\eta}$ provided by the simulator will propagate to the response matrix, and during the Bayesian iteration process using the response matrix, the error will propagate to the modulation degree of the corrected data.

The error propagation at Point 1 was calculated using the RooUnfold package. For the statistical error of the data and points 1 and 2, owing to the dependence of the Bayesian method iteration process on the original data, the contributions of these two parts are difficult to decouple and analyze. Therefore, a unified error estimation is provided by using the modified bootstrap method, and this part of the error is denoted by σ_{unfold}. Sampling was performed 10,000 times at a certain degree of polarization (using fully polarized data as an example).

1. Each sampling involved 100,000 with-replacement samplings of the data at 0°, 30°, 60°, 90°, 120°, and 150° phases in the experiment.
2. The sampled data at the six phases were reconstructed, and the Bayesian method was used to correct the reconstructed angular distribution results. Six sets of corrected data were fitted to obtain six modulation degrees.
3. Random weights were assigned to the six modulation degrees, with the total sum of the six weights equaling 1. The weighted sum yielded the modulation degree for this sampling.

After 10,000 samplings, the distribution of the modulation degrees was plotted and a Gaussian fit was applied. The fitted sigma value is σ_{unfold}. Figure 17 illustrates the modulation distribution of several energy points sampled using the modified bootstrap method from completely polarized data and σ_{unfold} obtained from Gaussian fitting.

For point 3, the error introduced by parameterization can be propagated to the error of the response matrix by providing the error of the parameter $\bar{\eta}$. This error ultimately propagates to a modulation degree error. The error introduced by parameterization is denoted by σ_{para}. We obtained the error of $\bar{\eta}$ by slightly adjusting the value of $\bar{\eta}$ corresponding to a specific energy point, denoted as $\Delta\bar{\eta}$. After the adjustment, we incorporated the parameters $\bar{\eta} + \Delta\bar{\eta}$ into Star-XP simulation software to simulate 1,500,000 events and reconstruct their angular distributions. When χ^2/ndf between the adjusted angular distribution and angular distribution obtained from the simulation with $\bar{\eta}$ was equal to one, $\Delta\bar{\eta}$ represented the estimated error of $\bar{\eta}$. We applied the modified bootstrap method to resample the data 10,000 times using the response matrix obtained from the parameter value $\bar{\eta} \pm \Delta\bar{\eta}$ and then performed Gaussian fitting to obtain the total error $\sigma_{\text{unfold+para}}$, denoted as σ_{sys}. contributions of the various error terms at different energy points and the corrected modulations are presented in Table 1.

Furthermore, we compared the variation trends of $\bar{\eta}$ and the ratio of the position resolutions in the Y and X directions of the detector at different energies, as shown in Fig. 18, and the trends agree well. Using existing calibration data, we collected data from unpolarized continuous X-ray sources in the energy range of 2.5–9.0 keV and performed reconstruction and correction. Based on the energy resolution of the detector and the energy points of the calibration, we divided the continuous spectrum into five intervals for correction, as shown in Fig. 19a and b. The residual modulation of the continuous spectrum decreased from 6.95% before correction to 0.22%. Figure 19c depicts the modulations at several energy points before [16] and after the Bayesian correction and compares them with the calibration results of the IXPE detector [43]. Comparing the modulations before and after correction, the modulations after correction are higher at each energy point. Comparing the corrected modulations with the results from IXPE, when the energy is below 4.51 keV, the modulations of our detector are lower than the IXPE calibration results. The charge induction chip pixel size of IXPE (60 µm) is smaller than the pixel size of our current Topmetal-II (83 µm), resulting in fewer pixel-reconstructed tracks for low-energy photons and higher reconstruction accuracy requirements for resolution. Therefore, the modulation of the reconstructed tracks for the low-energy part is lower than that of the IXPE results. However, when the energy is higher than 4.51 keV, the corrected modulations are higher than the IXPE results, possibly because of the better signal-to-noise ratio of Topmetal-II. For longer tracks, the pixel resolution no longer plays a decisive role in reconstruction accuracy, and factors such as chip noise, the diffusion coefficient of secondary

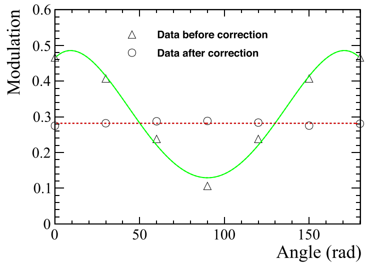

(a) 2.98 keV

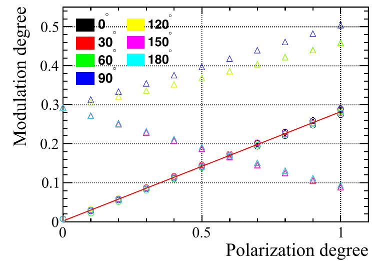

(b) 2.98 keV

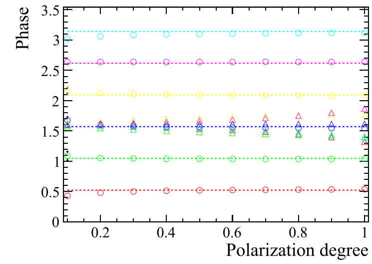

(c) 2.98 keV

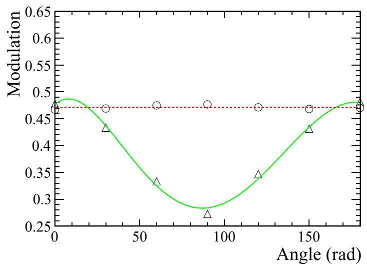

(d) 4.51 keV

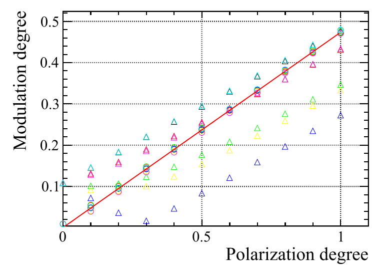

(e) 4.51 keV

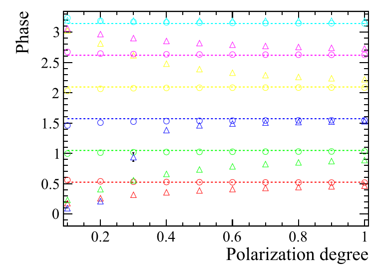

(f) 4.51 keV

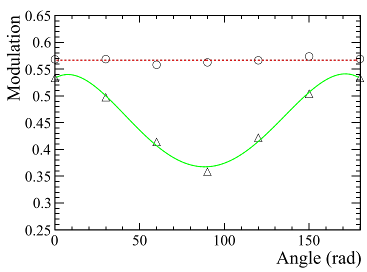

(g) 5.40 keV

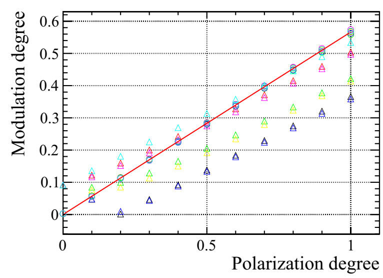

(h) 5.40 keV

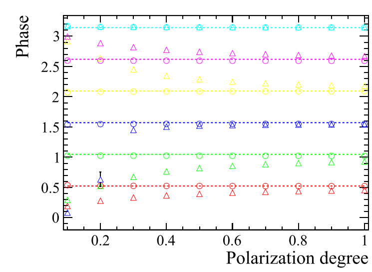

(i) 5.40 keV

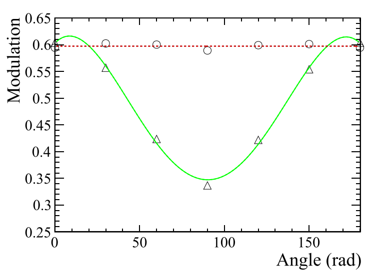

(j) 6.40 keV

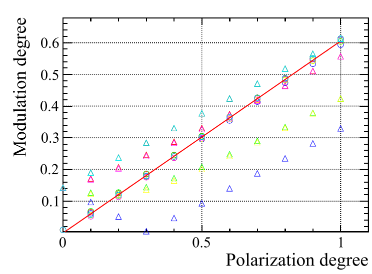

(k) 6.40 keV

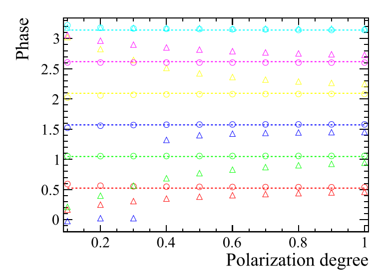

(l) 6.40 keV

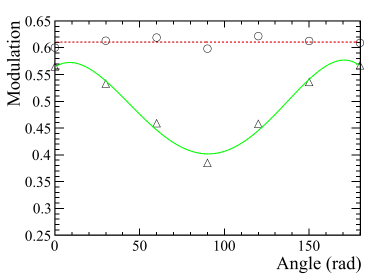

(m) 8.05 keV

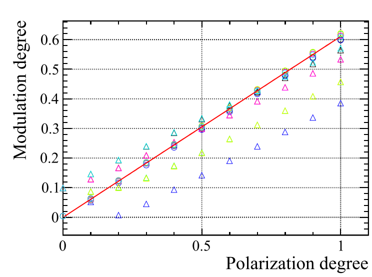

(n) 8.05 keV

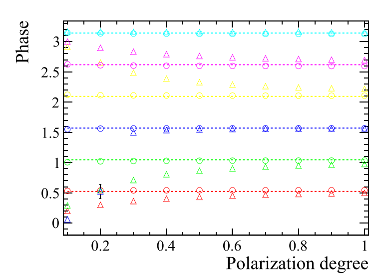

(o) 8.05 keV

◀**Fig. 16** (Color online) Results for 2.98 keV, 4.51 keV, 5.40 keV, 6.40 keV, and 8.05 keV, respectively. **a**, **d**, **g**, **j**, and **m** present the modulation degree measured at different polarization phases of polarized sources and the corrected modulation degree. **b**, **e**, **h**, **k**, and **n** present the comparison before and after correction for data at different polarization phases and degrees. The hollow triangles represent the uncorrected results, the hollow circles represent the corrected results, with different colors representing different polarization phases, and the red line represents the linear fitting of the corrected data. **c**, **f**, **i**, **l**, and **o** present the reconstruction of the polarization phase before and after correction, with the dashed line representing the true polarization phase of the polarized source

ionization electrons, detector gain, track length, and others begin to have a greater impact on the reconstruction. More importantly, after the correction, the residual modulations of the detector at several energy points have been reduced to levels below 1%. In addition, the residual modulation results at 5.90 keV in Fig. 19d were obtained using $\bar{\eta}$ at 5.40 keV. The result of the response matrix correction at 5.90 keV is 0.24% ± 0.59%. The energy resolution at 5.40 keV, corresponding to the detector, is approximately 19.5% [16] and 5.90 keV coincides with the boundary value of the 5.40 keV energy resolution. This result indicates that the calibration parameter $\bar{\eta}$ can be extended to the energy resolution range of the detector at several energy points while maintaining good correction results.

5 Summary and outlook

This paper discusses the systematic effects of the GMPD and corrects the residual modulation of modulation curves caused by various systematic effects. The GMPD is a prototype detector designed for POLAR-2/LPD, and the study of the GMPD systematic effects is vital to the subsequent design and performance optimization of the LPD, the reduction of systematic effects, and the calibration of detector polarization performance. We list several main systematic effects that lead to residual modulation, including differences in the gain and layout of chip pixels, signal attenuation in electronics, track truncation, and charge accumulation effects. We corrected these known systematic effects through calibration, setting the threshold conditions, and time positioning. For the remaining residual modulation caused by part of the systematic effects, we obtained the response matrix through parameterization combined with Monte Carlo simulation and used the Bayesian method to eliminate the contribution of residual modulation in the modulation curve. The final results show that the residual modulation of the data corrected by our algorithm has been reduced to below 1% at various calibration energy points. The reconstructed modulation degrees of the data at different polarization phases exhibit good consistency, and the polarization and modulation degrees exhibit a good linear relationship. In addition, we discuss the errors in the correction algorithm proposed in this paper and compare the corrected modulation results with the IXPE calibration results. The GMPD data results after correction using our algorithm show better polarization detection performance than IXPE above 5 keV.

The results of this study indicate that the proposed correction algorithm can be applied to correct systematic effects in the LPD. Additionally, our parameterized correction algorithm can be extended to the study and correction of the systematic effects of oblique incidence. A correction algorithm that introduces Stokes parameters in IXPE is established under normal incidence. When photons are obliquely incident, the description of photoelectrons using the Stokes parameter system is incomplete [44], which makes it difficult to extend it to the correction of oblique incidence systematic errors. The large-field-of-view design of the LPD implies that most of the time we must analyze obliquely incident data results. Based on the method proposed in this paper, we will conduct reconstruction and study the systematic effects of oblique incidence in future.

Appendix A: Bayesian iterative method

The Bayesian iterative method is a statistical technique used to estimate a probability distribution by iteratively updating prior beliefs using new evidence. It is employed to correct for detector effects and estimate the true distribution of a physical variable from the measured data.

In the Bayesian method, the unfolded distribution, $\hat{n}(C_i)$, is obtained by applying the unfolding matrix M_{ij} to the measured distribution $\hat{n}(E_j)$, as shown in Eq. A1:

$$\hat{n}(C_i) = \sum_{j=1}^{n_{\mathrm{E}}} M_{ij} n(\mathrm{E}_j). \tag{A1}$$

The unfolding matrix is given by

$$M_{ij} = \frac{P(E_j|C_i)n_0(C_i)}{\epsilon \sum_{k=1}^{n_{\mathrm{C}}} P(E_j|C_k)n_0(C_k)}. \tag{A2}$$

$P(E_j|C_k)$ is the element of response matrix R. ϵ is defined as $\epsilon_i \equiv \Sigma_{j=1}^{n_E} P(E_j|C_i)$. In the first round of Bayesian iterations, $n_0(C)$ is set based on prior knowledge, whereas in subsequent iterations, $n_0(C)$ is replaced by $\hat{n}(C)$ obtained from Eq. A1. $\hat{n}(C)$ is updated at each iteration.

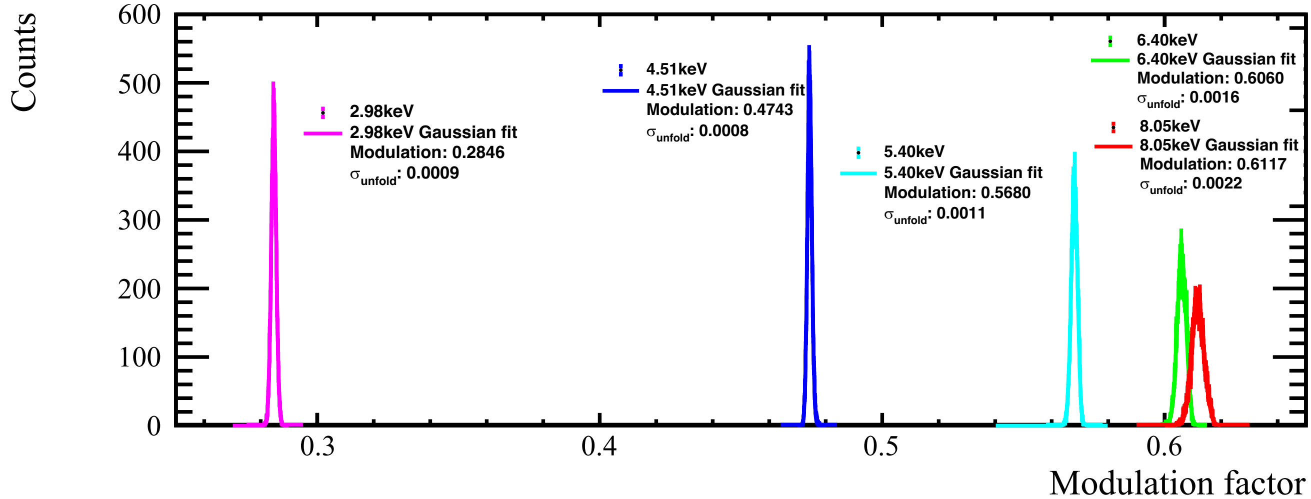

Fig. 17 (Color online) Modified bootstrap method used to sample datasets at different energy points, which are then iteratively corrected through Bayesian inference to obtain the weighted modulation degree distribution. The modulation degree distribution is estimated by fitting it with a Gaussian function to quantify the error introduced by the Bayesian iteration, denoted as σ_{unfold}

The computation of the error propagation matrix using the Bayesian method is given by Eqs. A3 and A4:

$$\frac{\partial \hat{n}(C_i)}{\partial n(E_j)} = M_{ij} + \sum_{k=1}^{n_E} M_{ik} n(E_k) \times \left(\frac{1}{n_0(C_i)} \frac{\partial n_0(C_i)}{\partial n(E_j)} - \sum_{l=1}^{n_C} \frac{\epsilon_l}{n_0(C_l)} \frac{\partial n_0(C_l)}{\partial n(E_j)} M_{lk} \right). \tag{A3}$$

$$V(\hat{n}(C_k), \hat{n}(C_l)) = \sum_{i,j=1}^{n_E} \frac{\partial \hat{n}(C_k)}{\partial n(E_i)} V(n(E_i), n(E_j)) \frac{\partial \hat{n}(C_l)}{\partial n(E_j)}. \tag{A4}$$

Here, $V(n(E_i), n(E_j))$ is computed from measurement data.

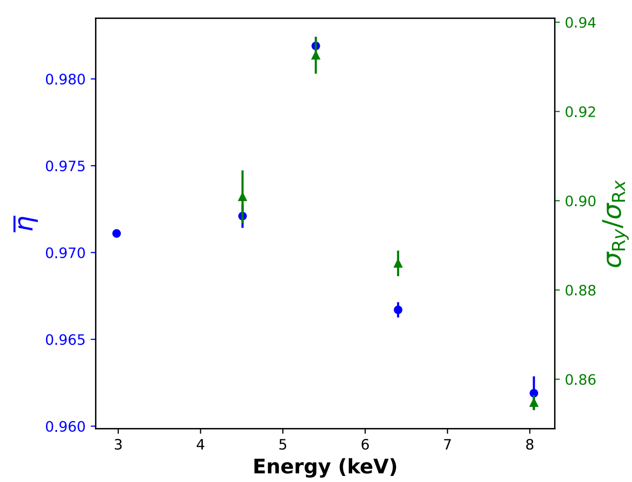

Fig. 18 (Color online) Comparison of the position resolution ratios in the Y (σ_{Ry}) and X (σ_{Rx}) directions with $\bar{\eta}$ at different energies. Blue circles represent $\bar{\eta}$, and green triangles represent $\sigma_{\text{Ry}}/\sigma_{\text{Rx}}$

Table 1 Values of $\bar{\eta}$, $\Delta\bar{\eta}$, σ_{unfold}, σ_{para}, and the statistical error σ_{stat} at different energy points, as well as the corrected modulations or residual of polarized and unpolarized source. The detailed parameters of the X-ray polarizing source can be found in [40]

Energy (keV)	$\bar{\eta}$	$\Delta\bar{\eta}$	σ_{unfold}	σ_{sys}	Polarization degree	σ_{stat}	σ_{total}	Modulation/ Residual
2.98	0.9711	0.00024	0.0009	0.0010	97.4%	0.0079	0.0080	0.2846
					0.0	0.0072	0.0073	0.0075
4.51	0.9721	0.00068	0.0008	0.0009	99.8%	0.0033	0.0034	0.4743
					0.0	0.0058	0.0059	0.0093
5.40	0.9819	0.00052	0.0011	0.0013	99.9%	0.0037	0.0039	0.5680
					0.0	0.0057	0.0058	0.0029
6.40	0.9667	0.00044	0.0016	0.0022	99.8%	0.0038	0.0044	0.6060
					0.0	0.0057	0.0061	0.0084
8.05	0.9619	0.00097	0.0022	0.0023	99.8%	0.0026	0.0034	0.6117
					0.0	0.0039	0.0045	0.0038

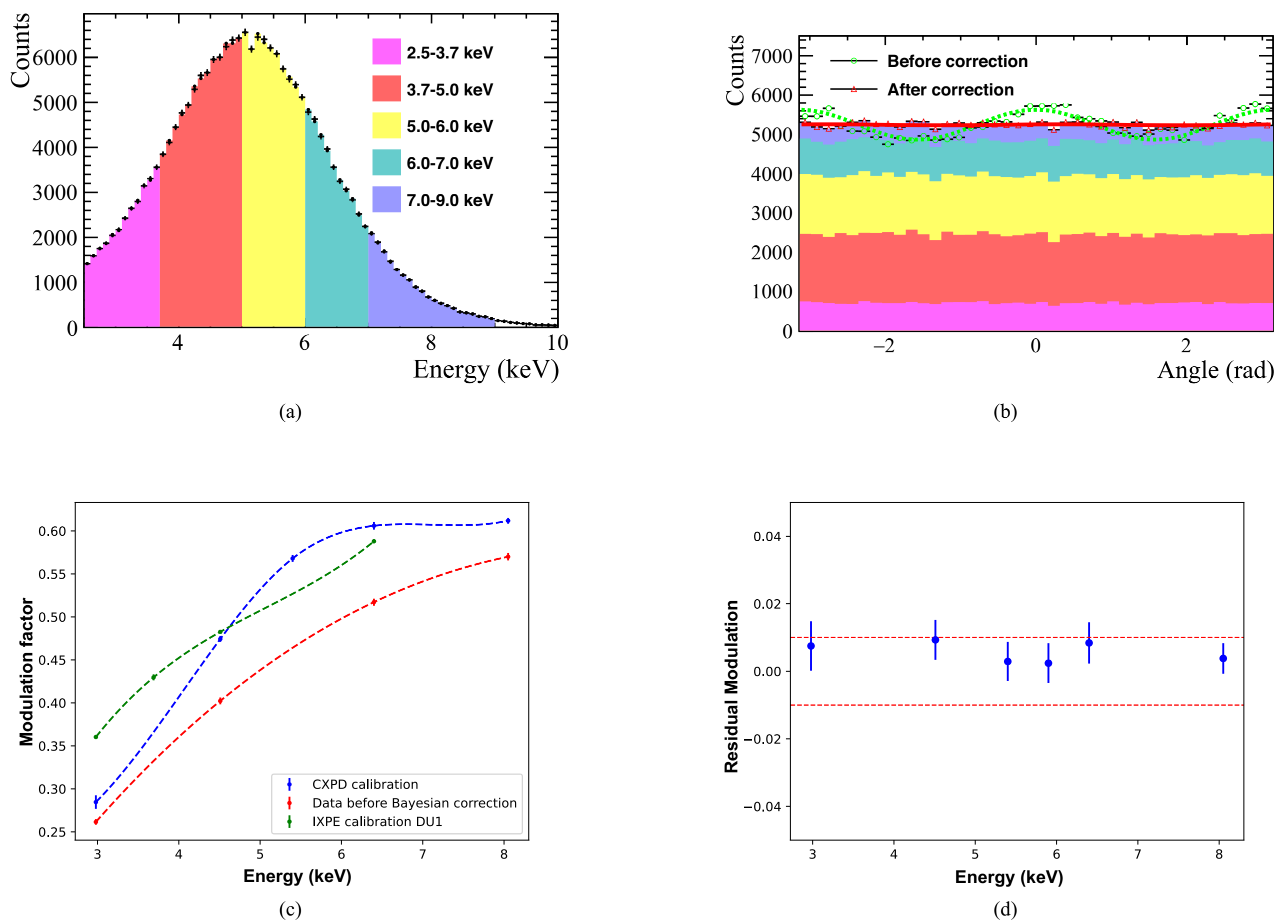

Fig. 19 (Color online) **a**, **b** Residual modulation of the continuous X-ray energy spectrum before and after partition correction. The green dashed line represents the fitting result of the residual modulation before correction, whereas the red solid line represents the fitting result after correction. **c** Red points represent the modulations at different energy points before correction [16], blue points represent the results after correction, and green points represent the calibration results of the IXPE Detection Unit 1 (DU1). **d** Residual modulation after correction of unpolarized data

Author Contributions All authors contributed to the conception and design of the study. Di-Fan Yi was responsible for method design, acquisition of experimental data, data analysis, and manuscript drafting. Qian Liu, Hong-Bang Liu, Fei Xie, and Jin Li provided suggestions on the content organization of this manuscript and the experimental protocol. Huan-Bo Feng assisted in the construction of the data acquisition platform and equipment debugging. Zu-Ke Feng offered support in data analysis. En-Wei Liang and Yang-Heng Zheng funded and supervised this research project. All authors have read and approved the final manuscript.

Data Availability The data that support the findings of this study are openly available in Science Data Bank at https://cstr.cn/31253.11.sciencedb.j00186.00950 and https://www.doi.org/10.57760/sciencedb.j00186.00950.

Declarations

Conflict of interest The authors declare that they have no conflict of interest.

References

1. J. Burgess, F. Cadoux, J. Greiner et al., Development and science perspectives of the POLAR-2 instrument: a large scale GRB polarimeter. arXiv preprint arXiv:2109.02978. https://doi.org/10.22323/1.395.0580
2. A.D. Angelis, M. Mallamaci, Gamma-ray astrophysics. Eur. Phys. J. Plus **133**, 324 (2018). https://doi.org/10.1140/epjp/i2018-12181-0
3. N. Produit, T. Bao, T. Batsch et al., Design and construction of the POLAR detector. Nucl. Instrum. Meth. Sect. A **877**, 259–268 (2018). https://doi.org/10.1016/j.nima.2017.09.053
4. P. Kumar, B. Zhang, The physics of gamma-ray bursts & relativistic jets. Phys. Rep. **561**, 1–109 (2015). https://doi.org/10.1016/j.physrep.2014.09.008
5. F.Y. Wang, Z.G. Dai, E.W. Liang, Gamma-ray burst cosmology. New Astron. Rev. **67**, 1–17 (2015). https://doi.org/10.1016/j.newar.2015.03.001
6. B. Zhang, P. Mészáros, An analysis of gamma-ray burst spectral break models. Astrophys. J. **581**, 1236 (2002). https://doi.org/10.1086/344338
7. D. Bégué, J.M. Burgess, The anatomy of a long gamma-ray burst: a simple classification scheme for the emission mechanism(s). Astrophys. J. **820**, 68 (2016). https://doi.org/10.3847/0004-637X/820/1/68
8. M. Rees, P. Mészáros, Unsteady outflow models for cosmological gamma-ray bursts. Astrophys. J. **430**, L93–L96 (1994). https://doi.org/10.1086/187446
9. K. Toma, T. Sakamoto, B. Zhang et al., Statistical properties of gamma-ray burst polarization. Astrophys. J. **698**, 1042 (2009). https://doi.org/10.1088/0004-637X/698/2/1042
10. R. Gill, J. Granot, P. Kumar, Linear polarization in gamma-ray burst prompt emission. Mon. Not. R. Astron. Soc. **491**, 3343–3373 (2019). https://doi.org/10.1093/mnras/stz2976
11. C. Lundman, A. Pe'Er, F. Ryde, Polarization properties of photospheric emission from relativistic, collimated outflows. Mon. Not. R. Astron. Soc. **440**, 3292–3308 (2014). https://doi.org/10.1093/mnras/stu457
12. D. Lazzati, E. Rossi, G. Ghisellini et al., Compton drag as a mechanism for very high linear polarization in gamma-ray bursts. Mon. Not. R. Astron. Soc. **347**, L1–L5 (2004). https://doi.org/10.1111/j.1365-2966.2004.07387.x
13. J. Granot, A. Königl, Linear polarization in gamma-ray bursts: the case for an ordered magnetic field. Astrophys. J. **594**, L83 (2003). https://doi.org/10.1086/378733
14. S.N. Zhang, M. Kole, T.W. Bao et al., Detailed polarization measurements of the prompt emission of five gamma-ray bursts. Nat. Astron. **3**, 258–264 (2019). https://doi.org/10.1038/s41550-018-0664-0
15. H.B. Feng, H.B. Liu, D. Wang et al., Gas microchannel plate-pixel detector for X-ray polarimetry. Nucl. Sci. Tech. **35**, 39 (2024). https://doi.org/10.1007/s41365-024-01407-3
16. H.B. Feng, H.B. Liu, Y.J. Xie et al., Spectral and polarimetric characterization of the gas microchannel plate pixel detector. J. Instrum. **18**, P08012 (2023). https://doi.org/10.1088/1748-0221/18/08/P08012
17. H. Feng, W. Jiang, M. Minuti et al., Polarlight: a CubeSat X-ray polarimeter based on the gas pixel detector. Exp. Astron. **47**, 225–243 (2019). https://doi.org/10.1007/s10686-019-09625-z
18. H. Li, H. Feng, F. Muleri et al., Assembly and test of the gas pixel detector for X-ray polarimetry. Nucl. Instrum. Meth. Sect. A **804**, 155–162 (2015). https://doi.org/10.1016/j.nima.2015.09.060
19. H. Feng, R. Bellazzini, The X-ray polarimetry window reopens. Nat. Astron. **4**, 547 (2020). https://doi.org/10.1038/s41550-020-1103-6
20. H. Li, X. Long, H. Feng et al., In-orbit operation and performance of the CubeSat Soft X-ray polarimeter *Polarlight*. Adv. Space Res. **67**, 708–714 (2021). https://doi.org/10.1016/j.asr.2020.09.001
21. H. Feng, H. Li, X. Long et al., Re-detection and a possible time variation of soft X-ray polarization from the crab. Nat. Astron. **4**, 511–516 (2020). https://doi.org/10.1038/s41550-020-1088-1
22. P. Soffitta, IXPE the imaging X-ray polarimetry explorer. Proceedings Volume 10397, UV, X-Ray, and Gamma-Ray Space Instrumentation for Astronomy XX, 103970I (2017). https://doi.org/10.1117/12.2275485
23. H. Wang, D. Wang, R. Chen et al., Electronics system for the cosmic X-ray polarization detector. Nucl. Sci. Tech. **34**, 64 (2023). https://doi.org/10.1007/s41365-023-01221-3
24. S. Zhang, A. Santangelo, M. Feroci et al., The enhanced X-ray timing and polarimetry mission-eXTP. Sci. China Phys. Mech. Astronom. **62**, 29502 (2018). https://doi.org/10.1007/s11433-018-9309-2
25. Z. Shen, J. Yu, B. Ma et al., Current progress of X-ray multilayer telescope optics based on thermally slumping glass for eXTP mission. Proceedings Volume 10699, Space Telescopes and Instrumentation 2018: Ultraviolet to Gamma Ray, 106991B (2018). https://doi.org/10.1117/12.2312629
26. P. Li, Q.Q. Yin, Z. Li et al., CATCH: chasing all transients constellation hunters space mission. Exp. Astron. **55**, 447–486 (2023). https://doi.org/10.1007/s10686-022-09879-0
27. J. Rankin, F. Muleri, A.F. Tennant et al., An algorithm to calibrate and correct the response to unpolarized radiation of the X-ray polarimeter onboard ixpe. The Astron. J. **163**, 39 (2022). https://doi.org/10.3847/1538-3881/ac397f
28. W.H. McMaster, Polarization and the stokes parameters. Am. J. Phys. **22**, 351–362 (1954). https://doi.org/10.1119/1.1933744
29. G. D'Agostini, A multidimensional unfolding method based on Bayes' theorem. Nucl. Instrum. Meth. Sect. A **362**, 487–498 (1995). https://doi.org/10.1016/0168-9002(95)00274-X
30. H. Feng, H. Liu, S. Liu et al., Charging-up effects for Gas Microchannel Plate detector. Nucl. Instrum. Meth. Sect. A **1055**, 168499 (2023). https://doi.org/10.1016/j.nima.2023.168499
31. C. Gao, G. Huang, X. Sun, Topmetal-II⁻: a direct charge sensor for high energy physics and imaging applications. J. Instrum. **11**, C01053 (2016). https://doi.org/10.1088/1748-0221/11/01/C01053

32. M. An, C. Chen, C. Gao et al., A low-noise CMOS pixel direct charge sensor, Topmetal-II-. Nucl. Instrum. Meth. Sect. A **810**, 144–150 (2016). https://doi.org/10.1016/j.nima.2015.11.153
33. W. Ren, W. Zhou, B. You et al., Topmetal-M: a novel pixel sensor for compact tracking applications. Nucl. Instrum. Meth. Sect. A **981**, 164557 (2020). https://doi.org/10.1016/j.nima.2020.164557
34. Z. Zhou, S.Q. Zhou, D. Wang et al., Low-noise and low-power pixel sensor chip for gas pixel detectors. Nucl. Sci. Tech. **35**, 58 (2024). https://doi.org/10.1007/s41365-024-01418-0
35. Z. Li, H. Feng, X. Huang et al., Preliminary test of topmetal-II- sensor for X-ray polarization measurements. Nucl. Instrum. Meth. Sect. A **1008**, 165430 (2021). https://doi.org/10.1016/j.nima.2021.165430
36. W.T. Grandy, *Quantum Theory of Radiation* (Springer, Netherlands, Dordrecht, 1991), pp. 204–241. https://doi.org/10.1007/978-94-011-3302-9_7
37. X.F. Huang, H.B. Liu, J. Zhang et al., Simulation and photoelectron track reconstruction of soft X-ray polarimeter. Nucl. Sci. Tech. **32**, 67 (2021). https://doi.org/10.1007/s41365-021-00903-0
38. T. Li, M. Zeng, H. Feng et al., Electron track reconstruction and improved modulation for photoelectric X-ray polarimetry. Nucl. Instrum. Meth. Sect. A **858**, 62–68 (2017). https://doi.org/10.1016/j.nima.2017.03.050
39. Z. Fan, H. Liu, H. Feng et al., Front-end electronics of CXPD for measuring transient X-ray sources. IEEE Trans. Nucl. Sci. **70**, 1507–1513 (2023). https://doi.org/10.1109/TNS.2023.3269091
40. Y. Xie, H. Liu, H. Feng et al., Variably polarized X-ray sources for LPD calibration. Exp. Astron. **56**, 499–515 (2023). https://doi.org/10.1007/s10686-023-09905-9
41. D.F. Yi, Q. Liu, R.T. Ma et al., Star-XP: a simulation framework for Polar-2/ low energy X-ray polarization detector. SoftwareX **25**, 101626 (2024). https://doi.org/10.1016/j.softx.2023.101626
42. Y.V. Bogomolov, V.V. Alekseev, O.A. Levanova et al., Review of unfolding methods. Phys. Usp. **66**, 628–642 (2023). https://doi.org/10.3367/UFNr.2022.05.039189
43. A.D. Marco, S. Fabiani, F.L. Monaca et al., Calibration of the IXPE focal plane X-ray polarimeters to polarized radiation. Astron. J. **164**, 103 (2022). https://doi.org/10.3847/1538-3881/ac7719
44. F. Muleri, On the operation of X-ray polarimeters with a large field of view. Astrophys. J. **782**, 28 (2014). https://doi.org/10.1088/0004-637X/782/1/28